

Magnus Hall Effect In Three-Dimensional Topological Semimetals

Sajid Sekh^{1,2} and Ipsita Mandal^{1,3}

¹*Institute of Nuclear Physics, Polish Academy of Sciences, 31-342 Kraków, Poland*

²*Department of Physics, Presidency University, 86/1 College Street, Kolkata-700073, India*

³*Department of Physics, Stockholm University, AlbaNova University Center, 106 91 Stockholm, Sweden*

Magnus Hall effect (MHE) is a non-linear Hall effect requiring no external magnetic field, which can be observed when an in-built electric field couples to the Berry curvature of the material, producing a current in the transverse direction. In this paper, we explore MHE in the context of various three-dimensional semimetals, incorporating various features like tilt, anisotropy, and multi-fold degeneracy. We numerically calculate the Magnus Hall conductivities and transport coefficients within the framework of Boltzmann transport theory. Although MHE was originally predicted for two-dimensional materials with time-reversal symmetry (TRS), we show that a finite Hall response is possible in materials without TRS. If TRS is preserved, broken inversion symmetry is needed to prevent the cancellation of Hall contribution over the Brillouin zone. In presence of anisotropic dispersions, we find that the MHE features differ depending on the directions of measurements (as expected), and the amount of tilt also greatly affects the conduction. Our investigations include MHE for multi-fold and nodal line semimetals as well. Our analysis is of great importance for transport measurements in experiments involving non-linear Hall effects.

Contents

I. Introduction	1
II. Review of the Derivation of the MHE	2
III. Magnus Hall Response for Various 3D Semimetals	4
A. Weyl Semimetal	4
B. Multi-Weyl Semimetals	5
C. Multi-fold Semimetals	7
D. Nodal Line Semimetals	8
IV. Discussions and Interpretation of the Results	9
V. Conclusion	10
References	10

I. Introduction

An electron, moving under the electric field inside a material and a perpendicular magnetic field, starts to drift due to Lorentz force, thus generating a current in the transverse direction. Discovered by Edwin Hall, this interplay of electric and magnetic field leads to the much-celebrated “classical Hall effect”. In a prototypical setup, the Hall voltage is directly proportional to the applied magnetic field and can be of few Tesla. If the strength of the magnetic field is further raised to 100 T, the Hall conductance becomes quantized, leading to integer [1] and fractional [2] quantum Hall effects. In this regime, several interesting phenomena are expected to occur, such as chiral edge states [3], and charge fractionalization [4]. These observations make the external magnetic field an essential ingredient of the Hall effect. But recent scientific endeavours suggest that Hall effects without a magnetic field are also possible, mainly through two ways – (1) either by adding spin or orbital degrees of freedom; (2) going beyond the linear response regime. The former route leads to quantum spin Hall effect [5] in a topological insulator (TI), where spin-orbit coupling acts as an artificial gauge field. The other avenue refers to the non-linear Hall effects which preserve time-reversal symmetry (TRS, denoted by \mathcal{T}), but require a broken inversion symmetry (denoted by \mathcal{I}). Mathematically, if the transverse Hall current \mathbf{J} is expanded in terms of the generating field \mathbf{E} , then the first-order (linear in the components \mathbf{E}) terms $\sigma_{ab} E_b$ refer to the linear Hall effect,

while the non-linear effect arises from the generation of spin currents as dictated by the second-order terms of the form $\chi_{abc} E_b E_c$ [6, 7]. To measure the non-linear current experimentally, an alternating current of low frequency is injected into the sample, which generates an oscillating voltage at ‘double-frequency’ in the case of non-linear Hall effect – a feature that is not present in its linear counterpart. Depending on the driving current (electrical, spin, or thermal) involved, non-linear Hall effects can be categorized into different types, namely non-linear spin Hall effect [8], gyrotrropic effect [9], Magnus Hall effect (MHE) [10–12], and non-linear Nernst effect [13, 14]. Several first-principle calculations predict such non-linear effects in the transition metal dichalcogenides [15, 16], crystalline topological insulators [17], and Weyl semimetals [18, 19]; while experimental observations exist in 2D layers of WTe₂ [20] and non-magnetic topological insulators Bi₂Se₃ [21].

In this paper, we focus on the MHE, which is a Berry curvature (BC) induced Hall effect requiring no external magnetic field. Classically, the Magnus effect is observed when a spinning object experiences a change in its trajectory while moving through a fluid, such that its path is deflected in a manner that is absent when the object is not spinning.

The MHE is the condensed matter analogue of the above, where chiral Bloch electrons, under an electrostatic potential gradient, develop a velocity in the transverse direction (cf. Fig. 1). The two main ingredients needed for MHE are: (1) a slowly varying potential gradient, which generates an in-built electrical field; and (2) a non-zero BC in the Brillouin zone. Symmetry-wise, in a system with broken TRS, BC satisfies $\Omega(\mathbf{k}) = \Omega(-\mathbf{k})$, which leads to an intrinsic anomalous Hall effect (AHE). However, in addition, there exist other types of materials where TRS is preserved, but spatial inversion symmetry is broken, leading to $\Omega(\mathbf{k}) = -\Omega(-\mathbf{k})$ with no AHE. Such symmetry configurations can be found in transition metal dichalcogenides [22], stacked graphene layers [23], and semimetals [24] where large BCs have been observed near the band-crossing points. Interestingly, recent proposals [10, 11] suggest TRS-invariant two-dimensional (2D) materials with broken inversion can, in fact, support finite Hall response. Here, we aim to show a similar mechanism that yields nonzero Magnus Hall response in three-dimensional (3D) semimetals as well, especially materials with broken TRS that have not been considered so far.

We consider topological semimetals with non-trivial BC to study MHE, as predictions of various anomalous and non-linear effects [25] already exist for such materials. Semimetals are characterized by their unique band-crossings in the Brillouin zone, which can either be point-like (Weyl semimetals), or along a curve (nodal line semimetals). Weyl semimetals are a 3D extension of the 2D Weyl cones, featuring isotropic linear dispersions. But in real materials, imperfections are ubiquitous, which tend to deform the isotropy of the dispersion. Deformations can occur in the form of anisotropy or tilt. In this article, we demonstrate how the presence or absence of particular deformations affects the MHE. For this purpose, we consider various semimetallic systems and compute the Magnus conductivities with possible factors such as anisotropy, tilt, and multi-fold crossings, to understand their roles in the MHE transport.

The paper is organized as follows. In Sec. II, we briefly review how the expression for MHE can be derived, using the Boltzmann transport formulation in the ballistic regime. The analyses for the various semimetallic Hamiltonians are shown in Sec. III. In particular, we start by discussing the MHE for TRS-broken materials in Sec. IIIA. In the next Sec. IIIB, we show how TRS invariance and anisotropy affect the MHE transport. We also show the features of MHE for multi-fold and nodal line semimetals in Sec. IIIC and Sec. IIID, respectively. In Sec. IV, we compare our results for the different semimetallic systems and discuss their implications. Finally, we end with a conclusion in Sec. V.

II. Review of the Derivation of the MHE

We consider a mesoscopic Hall slab 3D space, with the orthogonal axes labelled as a , b , and c . In particular, the slab is assumed to be extended infinitely in the \hat{a} direction, but has a finite width along \hat{b} . We then apply a slowly varying potential energy across its length (i.e. along \hat{a}). This introduces a bias voltage ΔU between two ends of the sample, namely the source and the drain, which creates an in-built electric field $\mathbf{E}_{in} = (\frac{1}{e} \partial_a U, 0, 0)$. Additionally, there is an applied electric field \mathcal{E}_{app} that drives the electrical current. The motion of the electrons in this Hall sample is dictated by the following two coupled equations:

$$\hbar \dot{\mathbf{r}} = \mathbf{v}_{band} + (\nabla_{\mathbf{r}} U + e \mathcal{E}) \times \Omega, \quad \hbar \dot{\mathbf{k}} = -\nabla_{\mathbf{r}} U - e \mathcal{E}_{app}, \quad (1)$$

where $\mathbf{v}_{band} = \nabla_{\mathbf{k}} \mathcal{E}$ is the band velocity, $\mathcal{E}(\mathbf{k})$ is energy dispersion, and Ω is the BC. The terms $\nabla_{\mathbf{r}} U \times \Omega$ and $\mathcal{E}_{app} \times \Omega$ define the Magnus velocity \mathbf{v}_{mag} and the anomalous velocity \mathbf{v}_{ano} , respectively. The Magnus velocity \mathbf{v}_{mag} arises for a bias voltage $\partial_a U$, as electrons that are moving from source to drain will get drifted towards \hat{b} due to the Magnus velocity $-\Omega_c \partial_a U \hat{b}$. This generates a Hall current proportional to the c -component of the BC, which can be estimated by measuring the transverse voltage [see Fig. 1]. We aim to understand the Hall conductivity for ballistic transport – a transport regime where scattering time τ is so large that effectively no collision takes place within the sample.

To calculate the Magnus Hall conductivities, we use the Boltzmann transport equation [26, 27], that describes the

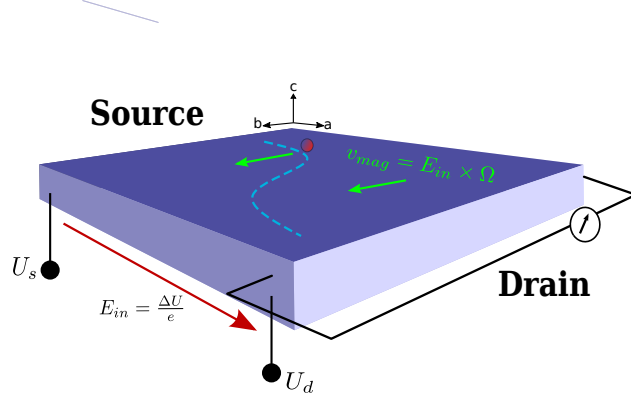


FIG. 1. A cartoon of the Magnus Hall setup is shown. Due to the bias voltage $\Delta U = U_s - U_d$ across the length of a Hall sample, an in-built electric field $\mathbf{E}_{in} = e^{-1} \nabla_a U \hat{a}$ develops between the source and the drain. This electric field couples to the Berry curvature in a way such that when an electron moves from the source to drain, it gets deflected toward \hat{b} , generating a current along that direction. This current can be measured by attaching probes in the transverse direction.

evolution of the distribution function $f(\mathbf{k}, \mathbf{r}, t)$ of the carriers as follows:

$$\left(\frac{\partial}{\partial t} + \dot{\mathbf{r}} \cdot \nabla_{\mathbf{r}} + \dot{\mathbf{k}} \cdot \nabla_{\mathbf{k}} \right) f(\mathbf{k}, \mathbf{r}, t) = I_{coll} \{f(\mathbf{k}, \mathbf{r}, t)\}. \quad (2)$$

The term on the right-hand side arises due to electron scattering and thus can be set to zero in the ballistic regime. We also restrict ourselves to the steady-state, so that $\partial f / \partial t = 0$. The carrier distribution function $f(\mathbf{k}, \mathbf{r}, t) = f_o + f_1$ is a sum of two terms, where f_o is the equilibrium part that is given by the Fermi distribution $f_o = \frac{1}{1 + e^{\frac{\tilde{\mathcal{E}}(\mathbf{k}, \mathbf{r}) - \bar{\mu}}{k_B T}}}$. with $\tilde{\mathcal{E}}(\mathbf{k}, \mathbf{r}) = \mathcal{E}(\mathbf{k}) + U(\mathbf{r})$, and $\bar{\mu}$ is the fixed (equilibrium) electrochemical potential. On the other hand, f_1 refers to the non-equilibrium part. For the expression of f_1 , we take an ansatz [10]

$$f_1(\mathbf{k}, \mathbf{r}) = \begin{cases} -\Delta\mu \partial_{\mathcal{E}} f_o - \frac{\tilde{\mathcal{E}}(\mathbf{k}, \mathbf{r}) - \bar{\mu}}{T} \Delta T \partial_{\mathcal{E}} f_o & \text{for } v_a > 0 \\ 0 & \text{for } v_a \leq 0 \end{cases}, \quad (3)$$

where μ is the total chemical potential. The ansatz is motivated through the fact that the bias voltage introduces an imbalance $\Delta\mu$ in the electrochemical potential between the source and the drain. Due to this imbalance, only electrons with $v_a > 0$ flows from source to drain, creating a steady current in the process. In addition, there exists a thermal gradient ΔT between the two ends, which leads to thermal conduction. Equipped with this, we can finally compute the electrical (\mathbf{J}) and thermal (\mathbf{Q}) currents using the expression

$$\{\mathbf{J}, \mathbf{Q}\} = \int \frac{d^3 k}{(2\pi)^3} \dot{\mathbf{r}} \{-e, \tilde{\mathcal{E}}(\mathbf{k}, \mathbf{r}) - \mu\} f_1(\mathbf{k}, \mathbf{r}, t). \quad (4)$$

Let us now consider a Hall set-up oriented in such a way that the Magnus current is in the \hat{b} -direction. For TRS-invariant materials, the anomalous contributions in Eq. (1) cancel out so that $\dot{\mathbf{r}}_a$ gets contributions from band-velocity and the Magnus term only. With this prescription, the electrical Hall current takes the form

$$J_b = -e \int \frac{d^3 k}{(2\pi)^3} \dot{r}_b f_1(\mathbf{k}, \mathbf{r}) = [\mathcal{J}_b + \mathcal{J}'_b]_{elec} + [\mathcal{J}_b + \mathcal{J}'_b]_{th}, \quad (5)$$

and yields electrical (superscript “elec”) and thermal (superscript “th”) current. Furthermore, each of these currents have two types of contributions— one from the Magnus velocity (primed) and another from the band-velocity (unprimed). Since the current densities have a spatial dependence, an integration over the sample length L is required, i.e., $I_b = \frac{1}{L} \int_0^L J_b$, which then can be compared with $\sigma_{ab} = \frac{e I_b}{\Delta\mu}$ to obtain the conductivity. Let us denote the electrical, Nernst, and thermal

conductivities by the symbols σ , α , and κ , respectively. The conductivities associated with the semi-classical band-velocity parts are then given by

$$\{\sigma_{ab}^o, \alpha_{ab}^o, \kappa_{ab}^o\} = -L \int \frac{d^3k}{(2\pi)^3} \left\{ e^2, -\frac{e(\mathcal{E} - \mu)}{T}, \frac{(\mathcal{E} - \mu)^2}{T} \right\} \partial_{\mathcal{E}} f_o. \quad (6)$$

On the other hand, the Magnus Hall conductivities take the form

$$\begin{aligned} \sigma_{ab}^m &= -\frac{e^2 \Delta U \epsilon_{abc}}{\hbar} \int_{v_a > 0} \frac{d^3k}{(2\pi)^3} \Omega_c \partial_{\mathcal{E}} f_o, \\ \alpha_{ab}^m &= \frac{e \Delta U \epsilon_{abc}}{\hbar T} \int_{v_a > 0} \frac{d^3k}{(2\pi)^3} \Omega_c (\mathcal{E} - \mu) \partial_{\mathcal{E}} f_o, \\ \kappa_{ab}^m &= -\frac{\Delta U \epsilon_{abc}}{\hbar T} \int_{v_a > 0} \frac{d^3k}{(2\pi)^3} \Omega_c (\mathcal{E} - \mu)^2 \partial_{\mathcal{E}} f_o, \end{aligned} \quad (7)$$

where $\Delta U = \int_0^L da (\partial U / \partial a)$ is the average potential difference along \hat{a} and ϵ_{abc} denotes cyclic permutation. In Eqs. (6) and (7), notations σ , α and κ denote electrical, Nernst and thermal conductivity, respectively. An important difference here is that, the coefficients in Eq. (6) are independent of ΔU , but Magnus Hall conductivities in Eq. (7) vary linearly with ΔU . Due to the factor $\partial_{\mathcal{E}} f_o$, states near the Fermi surface take part in conduction. More explicitly, the conduction depends on the carriers with $v_a(\mathbf{k}) > 0$ in the vicinity of the Fermi surface, and how they activate the Berry curvature. If the Fermi energy is much higher than the thermal energy, then σ_{ab}^m , α_{ab}^m and κ_{ab}^m are related to each other by the Wiedemann-Franz law and Mott relation, as shown below

$$\alpha_{ab}^m = \frac{\pi^2 k_B^2 T}{3e} \frac{\partial \sigma_{ab}^m}{\partial \mu}, \quad \kappa_{ab}^m = \frac{\pi^2 k_B^2 T}{3e^2} \sigma_{ab}^m. \quad (8)$$

An important feature is that each transport coefficient is an odd function of μ . This means that either lowering or raising the Fermi level is sufficient to obtain the same magnitude of the response, albeit with opposite sign. For this reason, we only consider the chemical potential cutting the valence bands.

III. Magnus Hall Response for Various 3D Semimetals

In this section, we present the numerical results for the Magnus Hall transport, considering different types of 3D semimetals. We have used *Mathematica* to compute the Magnus Hall conductivities. In particular, we have used the spherical polar coordinates, and the ‘GlobalAdaptive’ strategy, to compute the integrals as a function of the chemical potential μ (with a scanning interval of 0.05 eV). For such numerical calculations, it is always important to make sure that the results do not depend on the unphysical parameters, such as the integration cut-off Fermi surface. Ideally, the cut-off is experimentally motivated. But since here we focus on a more general description of semimetals (based on low-energy continuum limits), instead of specific materials, we have chosen the cut-off Fermi surface through a trial and error process, and have checked the convergence manually. We have also used the natural units, by setting $\hbar = c = e = 1$ throughout, for the sake of simplicity.

A. Weyl Semimetal

Weyl semimetallic phases depend on breaking of either \mathcal{T} or \mathcal{I} symmetry, or both. As a first step, \mathcal{T} -broken semimetals are easiest to think of, since they hold the minimum number of Weyl nodes, resulting in a total of two nodes of opposite chirality. In order to discuss the MHE in the absence of \mathcal{T} symmetry, we consider a 2×2 Weyl Hamiltonian given by [25]

$$\mathcal{H} = v_F \boldsymbol{\sigma} \cdot \mathbf{d}_{\mathbf{k}}, \quad (9)$$

where $\boldsymbol{\sigma}$ is the vector of the three Pauli matrices, $\mathbf{d}_{\mathbf{k}} = \{k_x, k_y, \frac{k_z^2 - \beta^2}{2\beta}\}$, and v_F (set to 1) is the Fermi velocity. The Hamiltonian parameter β separates the Weyl nodes in the momentum space, so that the band-crossing points occur at $(0, 0, \pm\beta)$ [see Fig. 2a)] – in particular, the two Weyl points are separated by a distance of 2β . Since unbounded linear

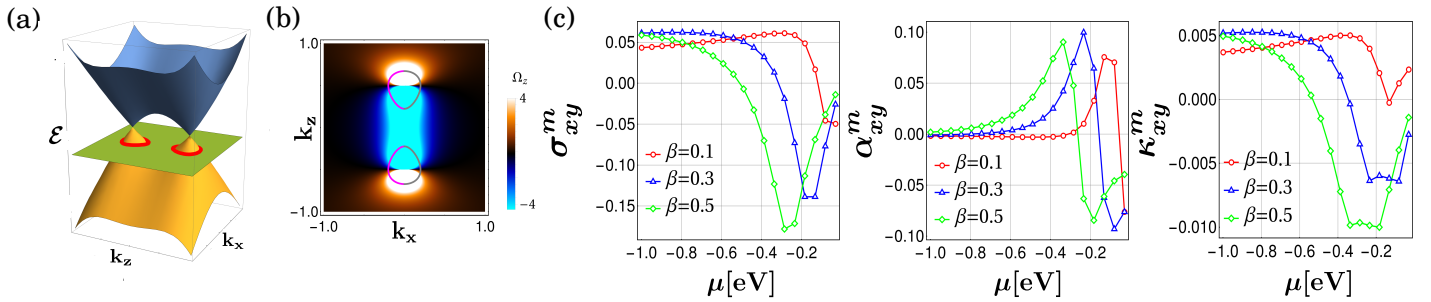


FIG. 2. (a) Energy dispersion of the Weyl Hamiltonian in Eq. (9) for $\mu = -0.2$ eV and $\beta = 0.5$ eV $^{-1}$, with the projection of the 3D Fermi surface highlighted in red. (b) The corresponding Berry curvature is shown, along with the superimposed projections of the Fermi surface contours in the $k_z - k_x$ plane. The latter is color-coded such that the states with $v_x > 0$ are in magenta, and those with $v_x < 0$ are in gray. (c) The Magnus Hall coefficients σ_{xy}^m (in units of $10^{-3}e^2/\hbar$), α_{xy}^m (in units of $10^{-3}ek_B/\hbar$), and κ_{xy}^m (in units of $10^{-3}k_B/\hbar$) are displayed as functions of μ , for three different values of β . Here, $\Delta U = 0.05$ eV and $T = 300$ K.

dispersion model is not realistic in solid state systems, we have used the model from Ref. [25], where band-bending effects have been introduced through modified crystal momenta.

The broken \mathcal{T} symmetry is easy to envision because of the node splitting, as Weyl points at $k_z = \pm\beta$ are of opposite chiralities, and do not obey the Kramer's theorem. The Fermi surface can be obtained by solving $\mathcal{E}(\mathbf{k}) = \mu$, where μ is the chemical potential and $\mathcal{E}(\mathbf{k}) \equiv \pm \epsilon_{\mathbf{k}}$ is the energy dispersion. Here, $\epsilon_{\mathbf{k}} = \sqrt{k_{\perp}^2 + k_{\parallel}^2}$, $k_{\perp} = \sqrt{k_x^2 + k_y^2}$, and $k_{\parallel} = \frac{k_z^2 - \beta^2}{2\beta}$. Note that the dispersion along k_z is taken to be quadratic here, in order to capture the ‘band-bending’ effect, that is ubiquitous in most realistic materials away from the band-crossing points. As we move to low energies ($\mathbf{k} \rightarrow 0$), higher-order terms become negligible and the dispersion is linear in all directions. Here we aim to compute the xy-component of the MHE conductivities so that the x-component of band-velocity (v_x) and the z-component of BC (Ω_z) are relevant. These can be expressed as:

$$v_x(\mathbf{k}) = \partial_{k_x} \mathcal{E}(\mathbf{k}) = \pm \frac{k_x}{\epsilon_{\mathbf{k}}}, \quad \Omega_z(\mathbf{k}) = \pm \frac{1}{4} \hat{\mathbf{d}}_{\mathbf{k}} \cdot (\partial_{k_x} \hat{\mathbf{d}}_{\mathbf{k}} \times \partial_{k_y} \hat{\mathbf{d}}_{\mathbf{k}}) = \pm \frac{k_{\parallel}}{2\epsilon_{\mathbf{k}}^3}, \quad \hat{\mathbf{d}}_{\mathbf{k}} = \frac{\mathbf{d}_{\mathbf{k}}}{|\mathbf{d}_{\mathbf{k}}|}. \quad (10)$$

In the Fig. 2(a), we show the band-structure for $\beta = 0.5$ eV $^{-1}$, with the projection of the Fermi surface shown in red color for $\mu = -0.2$ eV. As mentioned earlier, the interplay of the Fermi surface and BC plays a central role in deciding the fate of the MHE response. This can be understood through Fig. 2(b), which shows the Fermi surface contours superimposed on the contour-plot for Ω_z in the zx-plane. The Fermi surface is color-coded according to its slope, such that the contributing states with $v_x > 0$ are in magenta, and the inert states with $v_x < 0$ are colored gray. When μ is at the Weyl points, the Fermi surface is point-like and exists at two points, $\pm\beta$. Upon lowering μ , the Fermi surface undergoes a topological Lifshitz transition, in the sense that two separate lobes merge into a single surface. It is useful to emphasize that any MHE response depends on the states near the Fermi surface, due to which a change in its topology dramatically affects the conductivities. We capture this in Fig. 2(c), where we plot σ_{xy}^m , α_{xy}^m , κ_{xy}^m as functions of μ , for $\beta = 0.1, 0.3$, and 0.5 . We see that for $\beta = 0.5$, σ_{xy}^m starts to increase, attaining a peak at the Lifshitz transition, and then falling off as the Fermi level is brought closer to zero. This is because, away from the Weyl nodes, the Fermi surface mostly activates vanishing BC, which leads to a small response. As μ is raised and brought closer to zero energy, although the Fermi surface shrinks, it activates larger values of BC, which in turn increases the response. Finally, the response decreases when μ is close to the nodes, which can be attributed to the cancellation of the contributions coming from Fermi pockets at that regime.

B. Multi-Weyl Semimetals

Ideally for Weyl-like excitations, the band-dispersion is linear in every direction in the low-energy limit. But this can be too strong of a constraint in real materials, and anisotropy may occur. One particular scenario is when the dispersion is either quadratic or cubic in the $k_x - k_y$ -plane, and linear dispersion along the k_z -direction, which we usually call ‘‘multi-Weyl’’ semimetals [28], which contain a higher monopole charge (total Chern number of either electron or hole band) than their isotropic counterparts. For example, a monopole charge of $J = 2$ (double-Weyl nodes) can be seen in HgCr_2Se_4 [29]

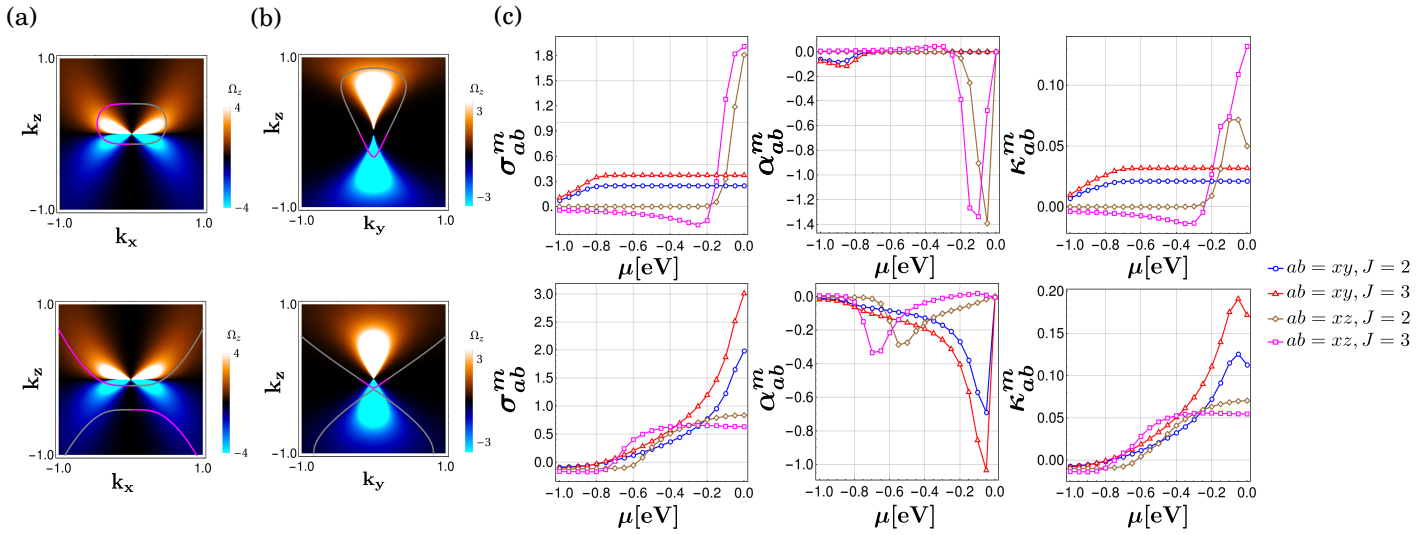


FIG. 3. Relevant Fermi surface projection ($\mu = -0.2$ eV), superimposed on the Berry curvature is shown for (a) xy and (b) xz -component of Magnus Hall conduction. Upper panel is for type-I phase ($\zeta = 0.5$) and lower panel is for type-II phase ($\zeta = 1.5$). Magneta color in Fermi surface refers to the states with $v_i > 0$ and gray means $v_i < 0$ [$i = x$ for (a) & z for (b)]. (c) Different components of Magnus Hall coefficients σ_{ab}^m (in units of $10^{-3}e^2/\hbar$), α_{ab}^m (in units of $10^{-3}ek_B/\hbar$), and κ_{ab}^m (in units of $10^{-3}k_B/\hbar$) are plotted against μ for $\zeta = 0.5$ (upper panel) and 1.5 (lower panel). Here we have taken $\Delta U = 0.05$ eV and $T = 300$ K.

and SrSi_2 [30], whereas materials with composition $A(\text{MoX})_3$ ($A = \text{Rb}, \text{Tl}; \text{X} = \text{Te}$) [31] harbours $J = 3$ monopole charge. They can also be found as BdG quasiparticles in the superconducting states of UPt_3 [32], SrPtAs [33], YPtBi [34]. We consider the general, low-energy Hamiltonian [35], which captures such anisotropy, as follows:

$$\mathcal{H} = \sum_a v'_{aa} k_a + \sum_{a,b} v_{ab} d_a(\mathbf{k}) \sigma_b, \quad d_x = k_\perp^J \cos(J\phi), d_y = k_\perp^J \sin(J\phi), d_z = k_z, \\ k_\perp = \sqrt{k_x^2 + k_y^2}, \quad \phi = \arctan(k_y/k_x), \quad (11)$$

where $a, b = \{x, y, z\}$ repeats over physical axes, and J is an integer that defines the order of the dispersion in the k_x - k_y -plane ($J = 2$ and $J = 3$ give quadratic and cubic dispersions, respectively). Here, we choose $v_{ab} = v_F \delta_{ab}$, with $v_F = 1$. The energy eigenvalues are given by $\mathcal{E}(\mathbf{k}) = \zeta k_z \pm \epsilon_{\mathbf{k}}$, with $\epsilon_{\mathbf{k}} = \sqrt{k_\perp^{2J} + k_z^2}$.

Here we consider a single cone with positive chirality, as the calculation is similar for other nodes. The first term in Eq. (11) signifies the tilting of the cone, and without any loss of generality, we consider this tilt along k_z by setting $v'_{aa} = \zeta \delta_{az}$. Thus tilting is tuned by a continuous parameter ζ . The Hamiltonian possesses \mathcal{T} (viz. $\mathcal{T}\mathcal{H}\mathcal{T}^{-1} = \mathcal{H}$), with $\mathcal{T} = \sigma_z \mathcal{K}$, but lacks \mathcal{I} along k_z as $\mathcal{H}(k_\perp, -k_z) = -\mathcal{H}(k_\perp, k_z)$. It is useful to note that since $d_a(\mathbf{k})$ directly affects the eigenspinors, any anisotropy in $d_a(\mathbf{k})$ is reflected in the BC and the Fermi surface. This implies that the values of the MHE transport coefficients will be different depending on which directions we are probing. With this in mind, here we illustrate both the xy - and xz -components of the MHE conductivities.

We are interested in finding the MHE response in different anisotropic directions, which can be either zero or finite, depending on the direction of tilt. This becomes apparent from the explicit expressions of the band-velocity $v(\mathbf{k})$, and the Berry curvature, $\Omega(\mathbf{k})$:

$$v(\mathbf{k}) = \left\{ \pm \frac{J k_\perp^{2(J-1)} k_x}{\epsilon}, \pm \frac{J k_\perp^{2(J-1)} k_y}{\epsilon}, \zeta \pm \frac{k_z}{\epsilon} \right\} \quad \Omega(\mathbf{k}) = \pm \frac{J k_\perp^{2(J-1)}}{2\epsilon^3} \{k_x, k_y, J k_z\}. \quad (12)$$

Because of TRS and broken \mathcal{I} , the components of the BC satisfies $\Omega_a \propto k_a$. Therefore, if we want to probe Ω_z , the k_x - k_z and k_y - k_z projections of the Fermi surface are relevant, as BC is non-zero in those planes. As a result, a tilt at least along the k_z -direction is needed to make the Fermi surface asymmetric, so that the MHE response does not get cancelled over the Brillouin zone. Similarly, we take tilt velocity $v'_{aa} = \zeta \delta_{ay}$ for the scenario when Ω_y is probed. Note that although the analysis with the xy -components in consideration has been done recently in Ref. [12], we have included it here for the sake of completeness.

We present our MHE results in Fig. 3(c) for both the xy - and xz -components. Although conductivity depends on a 3D integral, the fate of the individual components solely relies on a single Fermi surface projection. For instance, for the case of the xy -component, the relevant Fermi surface projections are in the k_x - k_z - and k_y - k_z planes, since Ω_z is probed. Out of these two, only k_x - k_z projection is important as v_x is zero in the k_y - k_z -plane. Similarly, for the xz -component of conductivity, only Fermi surface projection in the k_y - k_z -plane is important. These two relevant planes are shown in Fig. 3(a) and (b). In the upper panel of Fig. 3(c), when the Fermi level is close to the node and the tilt is sub-critical, the xy -component of the Hall response is nearly constant but the xz -component rises dramatically. This contrasting behaviour can be traced back from the Fig. 3(a) and (b), which shows a stark difference in relevant Fermi surface in each case. We also notice the response is always larger for cubic anisotropy, as BC strength is proportional to the order of anisotropy. Increasing the amount of tilt from $\zeta = 0.5$ to $\zeta = 1.5$, overtilts the cone and makes the Fermi surface open. This affects the MHE response in that, the xy -component which was constant earlier, now steadily rises as $\mu \rightarrow 0$. But the xz -component remains small owing to the small active Fermi surface.

C. Multi-fold Semimetals

Going beyond the two-band semimetals discussed so far, we now focus on multiple band-touching points in the Brillouin zone, which we generically call multi-fold semimetals. The band degeneracy point of such semimetals is predicted to host excitations of higher-pseudospin fermions, with no analogues in high-energy physics. So far excitations with pseudospin values $s = 1$ and $s = 3/2$ have been observed. The latter is also known as Rarita-Schwinger-Weyl semimetals (RSW) [36, 37]. Experimental observations include signatures of three-fold degeneracy point at the center of the Brillouin zone in CoSi [38], and a combination of three-fold and four-fold degeneracies at the Γ and R points of RhSi [39]. The linearized $\mathbf{k} \cdot \mathbf{p}$ Hamiltonian for such systems can be written as:

$$\mathcal{H} = \zeta k_z + \mathbf{k} \cdot \mathbf{S}, \quad (13)$$

where \mathbf{S} refers to the vector of the three pseudospin matrices. In the first term, we consider an \mathcal{I} -broken tilt term along k_z to generate asymmetry in the Fermi surface.

For $s = 1$, the dispersion $\mathcal{E}(\mathbf{k}) = 0, \pm k$ includes three bands. Out of these three, two are topological with Chern numbers $C = \pm 1$, and one is a trivial flat-band with $C = 0$. Owing to the flat-band, which does not take part in transport, the transport mechanism of pseudospin-1 fermions is essentially similar to a two-band model. On the other hand, the RSW case with $s = 3/2$ case has four topological bands with $C = \pm 1, \pm 3$, resulting in a high monopole charge of

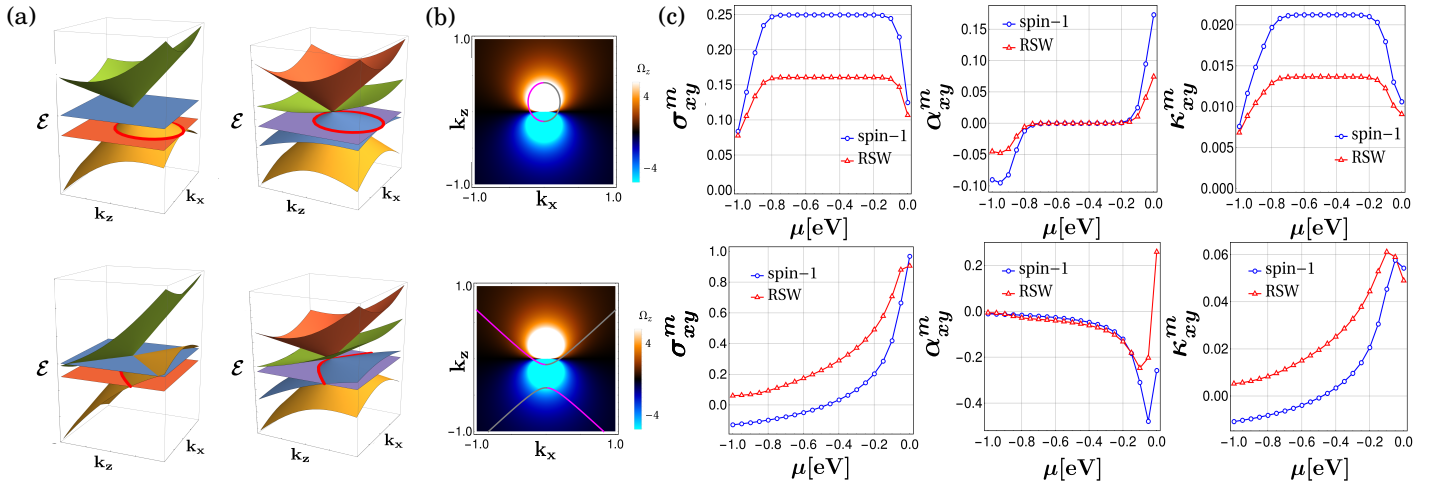


FIG. 4. (a) Dispersions of the pseudospin-1 and RSW semimetals are displayed side by side for $\mu = -0.2$ eV (with $\zeta = 0.5$ and $\zeta = 1.5$ for the upper and lower panels, respectively). (b) Fermi surface contour superimposed on the Berry curvature is shown for pseudospin-1 fermions. The projected Fermi surfaces use similar color-coding as the earlier figures. (c) The MHE coefficients σ_{xy}^m (in units of $10^{-3} e^2/\hbar$), α_{xy}^m (in units of $10^{-3} e k_B/\hbar$), and κ_{xy}^m (in units of $10^{-3} k_B/\hbar$) are displayed as functions of μ . The upper panel is for type-I phase ($\zeta = 0.5$), and lower panel is for the type-II phase ($\zeta = 1.5$). Here, $\Delta U = 0.05$ eV and $T = 300$ K.

magnitude 4. We can compactly write the band-velocity and BC as

$$v_x^p = p \frac{k_x}{2k}, \quad \Omega_z^p = \pm p \frac{k_z}{2k^3}, \quad (14)$$

respectively. Note that $p = 2$ for the pseudopseudospin-1 system, and $p = \{1, 3\}$ for the RSW Hamiltonian.

The band-structures, projected Fermi surfaces, BCs, and MHE responses are shown in Fig. 4. Naively, one would expect the MHE conductivities to be larger due to the presence of more bands. However, our results, as shown in Fig. 4(c), indicate that this is not always true. For example, even though RSW has more bands than the pseudospin-1 model, only two out of the four bands essentially participates in conduction, when tilting is small (i.e. in the type I phase). The higher-energy bands practically do not influence the MHE response, as they are too high up in energy and have zero fermi surface projections. Moreover, for RSW fermions, the bands responsible for conduction have a BC that is half compared to the pseudospin-1 bands. As a result, the MHE response for pseudospin-1 is larger than RSW fermions in the type-I phase, for a representative value of $\zeta = 0.5$. However, tuning to the type-II phase changes the scenario drastically. Over-tilting the cones make all the bands have nonzero Fermi surface projections, and as expected, the MHE conductivities of RSW fermions are larger than those of the pseudospin-1 fermions in this regime.

D. Nodal Line Semimetals

In addition to semimetals with bands crossing at a point, other classes of semimetals are possible where band-touching occurs along a nodal line. These are known as nodal line semimetals (NLSMs). The nodal ring of such materials can be protected by chiral \mathcal{C} , mirror \mathcal{M} , or a composite of particle-hole and time-reversal symmetry (denoted by \mathcal{PT}). However, all of these symmetries force the BC to vanish [40], and a mass term is typically needed to make the BC non-trivial. This mass term can appear in the form of weak spin-orbit coupling (SOC). In presence of the SOC, an extra glide symmetry is needed, along with \mathcal{T} and \mathcal{P} , to protect the nodal lines SrIrO₃ [41, 42]. For our purpose, we consider a minimal two-band Hamiltonian [43] with SOC, that has a single nodal line as follows:

$$\mathcal{H} = \lambda (k_\perp^2 - k_o^2) \sigma_x + v k_z \sigma_y + \Delta \sigma_z, \quad (15)$$

where the first term depicts a circular node $k_x^2 + k_y^2 = k_o^2$ in the k_x - k_y plane, and Δ is the strength of the SOC. Unlike \mathcal{T} -invariant materials, here we do not require tilt to observe finite MHE. This is because owing to the underlying symmetry of the Hamiltonian, BC is either positive or negative over the entire Brillouin zone, and there is no scope for internal cancellations [see Fig. 5b)]. For $\Delta = 0$, the Hamiltonian exhibits two discrete topological symmetries – (1) \mathcal{C} , with a representation of σ_z , which acts as $\mathcal{C} \mathcal{H} \mathcal{C}^{-1} = -\mathcal{H}$, and (2) \mathcal{PT} with a representation of $\sigma_x \mathcal{K}$ (\mathcal{K} is complex conjugation), which acts as $(\mathcal{PT}) \mathcal{H} (\mathcal{PT})^{-1} = \mathcal{H}$. Since our interest is in the low-energy states, the above Hamiltonian can be linearized by a transformation into the toroidal coordinates as follows:

$$k_x = (k_o + k \cos \phi) \cos \theta, \quad k_y = (k_o + k \cos \phi) \sin \theta, \quad k_z = k \frac{\sin \phi}{\alpha}, \quad (16)$$

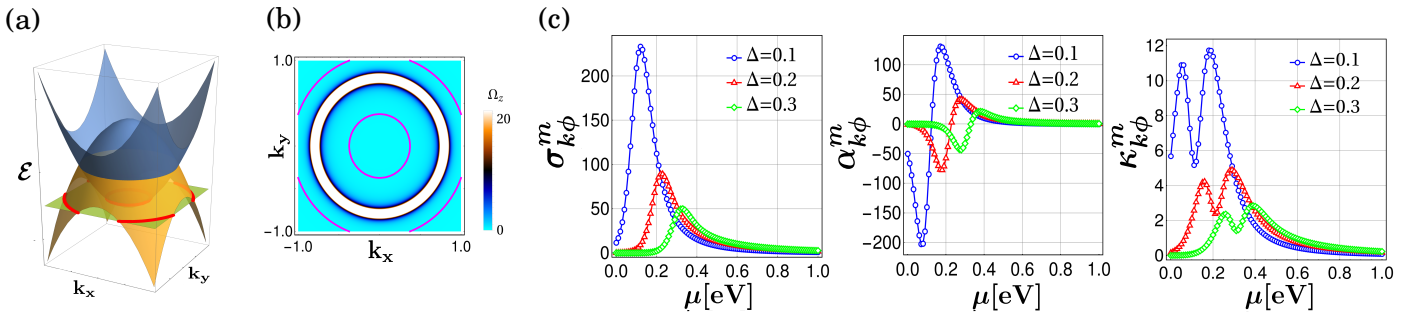


FIG. 5. (a) Dispersion of the nodal line semimetal, given by Eq. (15) for $\mu = -0.5$ eV. The Fermi level is shown in red. (b) The density plot of the θ -component of the BC is shown, along with the projection of the Fermi surface. Here magenta color refers to the Fermi states with $v_k > 0$. (c) The MHE coefficients $\sigma_{k\phi}^m$ (in units of $10^{-3} e^2/\hbar$), $\alpha_{k\phi}^m$ (in units of $10^{-3} e k_B/\hbar$), and $\kappa_{k\phi}^m$ (in units of $10^{-3} k_B/\hbar$) are plotted against μ for different Δ . Here, we have used the parameter values $\Delta U = 0.05$ eV and $T = 300$ K, $v = 2$, $k_o = 0.8$ eV⁻¹, and $\lambda = 1$ eV.

where k is radius of the toroid, k_o is the radius of the toroid from its center, $\alpha = v/v_o$, and $v_o = 2\lambda k_o$. Neglecting $\mathcal{O}(k^2)$ terms yields the linearized Hamiltonian

$$\mathcal{H} = v_o k (\cos \phi \sigma_x + \sin \phi \sigma_y) + \Delta \sigma_z. \quad (17)$$

The dispersion is given by $\mathcal{E}_\pm = \pm \sqrt{(\hbar v_o k)^2 + \Delta^2}$, where $k \simeq \frac{(k_x^2 + k_y^2 - k_o^2)^2}{4k_o^2} + \alpha^2 k_z^2$. The SOC acts like a mass term, thereby induces a gap of 2Δ along the nodal lines.

An important feature of the NSLM is that only one component of BC is non-zero, making it impossible to get a Magnus effect through orthogonal rotation of the external field or the Hall sample. In particular, one can show that a non-zero BC component $\Omega_\theta = \frac{\Delta_o}{2(k^2 + \Delta_o^2)^{3/2}}$ only along the toroidal direction $\hat{\theta}$. The quantity $\Delta_o = \Delta/v_o$ represents the scaled SOC strength, which suggests that $\Omega_\theta \rightarrow 0$ as $\Delta \rightarrow 0$. Interestingly, we note that $v_k = \hbar^2 v_o^2 k / \mathcal{E}_\pm$, which indicates that $v_k > 0$ for the upper band [see Fig. 5(b)]. Equipped with this, we can focus on a positive value of the chemical potential, and compute the conductivities for currents along the polar angle ϕ . Our results, as demonstrated in Fig. 5(c), indicate that Δ plays a central role in determining the strength of the MHE response. Especially, the MHE conductivities jump by at least a factor of two as Δ changes from 0.1 to 0.2, indicating that a weaker SOC yields a higher MHE response. This is because, a stronger SOC broadens the band-gap, which reduces the number of available states near the Fermi surface, and ends up suppressing the response. We also point out that most of the finite response is seen close to the nodal line since, at higher energies, the chemical potential cuts the band-edges, where the Fermi surface is non-existent. Notice that $\sigma_{k\phi}^m$ and $\kappa_{k\phi}^m$ have different profiles when the Fermi level is close to zero energy. This disagreement is expected since both the Wiedemann and Mott relations do not hold in this limit. This is because of higher temperatures ($T = 300$ K), and μ being comparable to the thermal energy $k_B T$.

IV. Discussions and Interpretation of the Results

In the subsections above, we have investigated the MHE in various 3D semimetals, showing how different factors (such as symmetry, anisotropy and tilt) affect the ballistic conduction within the Boltzmann transport theory. A non-zero response is obtained when the non-zero BC of the material couples to the in-built electric field to produce transverse Hall voltage. Being a conductive property, MHE response depends on a finite projection of the Fermi surface. However, the fate of the response also hinges on the slope of the Fermi surface, and how it activates the BC. If the BC is odd in \mathbf{k} , which is true for \mathcal{T} -invariant and \mathcal{P} -broken materials, then having a symmetric Fermi surface exactly cancels the contribution of the left ($-\mathbf{k}$) and right ($+\mathbf{k}$) moving carriers. However, tilting the cone makes the Fermi surface asymmetric, thus preventing this exact cancellation. This makes the MHE a useful quantity to probe tilt in topological semimetals. Additionally, in presence of \mathcal{T} , there is a vanishing band-velocity (since it depends on $\partial_{\mathcal{E}} f_o$) as well as a zero anomalous contribution, so that the conductivity entirely depends on the MHE contribution.

Most semimetallic phases occur at low-symmetry points of the Brillouin zone, where anisotropy is generic. Due to space-group symmetry, the anisotropic multi-Weyl dispersions are either quadratic or cubic in the k_x - k_y plane, and linear along k_z . This anisotropy is reflected in the Fermi surface and the relevant component of the BC, which makes the components of the Hall conductivity tensor unequal. For instance, a contrasting MHE response can be seen in our result when the Fermi level is close to the node and the tilt is sub-critical. We find that the xy -component of MHE response stays constant, while the zx -component sharply rises. Changing the non-linear dispersion from quadratic ($J = 2$) to cubic ($J = 3$) simply increases the strength of the response, since the components of BC are proportional to either J or J^2 . Going beyond the critical point also increases the response, as electron-hole pockets form at the Fermi surface. Based on this, we expect the MHE to be weak in \mathcal{T} -invariant TaAs class of materials possessing type-I Weyl quasiparticles, while type-II semimetals like WTe₂, MoTe₂, WP₂ and Ta₃S₂ should have pronounced MHE effects [44].

Recently discovered chiral materials like RhSi and CoSi, representing the multi-fold semimetals, can also display MHE. The overall trends of MHE response and its dependence on tilt in these systems, are reminiscent of a \mathcal{T} -invariant Weyl cones, as both share similar Fermi surface and BC behaviour. The only difference is that multifold semimetals have more bands near the band-crossing point that can participate in the conduction while in the type II phase, making MHE stronger than its two-band Weyl counterparts.

We have also shown that the requirement of tilt is not always necessary. This is true for \mathcal{T} -broken materials where BC is either positive or negative throughout the Brillouin zone, and thus symmetric cancellations cannot occur. But the absence of \mathcal{T} symmetry leads to non-zero anomalous Hall effects. It is useful to note that the anomalous conductivity for Weyl semimetal is proportional to the separation between the Weyl points [42]. Interestingly, our result shows increasing the distance between the Weyl node, amplifies the MHE. This makes it tricky to measure MHE in \mathcal{T} broken materials. Examples include WP₂ and MoP₂, which have a large separation in their Weyl points, and in principle, anomalous

contributions can mask the MHE signatures. A more realistic calculation of different Hall contributions within a lattice framework will be more illuminating in this regard.

V. Conclusion

The intrinsic contribution to the MHE, which is a non-linear Hall effect, has a geometric nature because of its connection to the Berry curvature. Consequently, it has opened up heretofore unexplored and promising prospects for future research in the area of topological phases, by driving the study of quantum transport and topological physics to the non-linear response regime. For such phenomena, the intrinsic part of the Hall conductivity tensor is related to the Berry curvature dipole [6]. The fact that MHE requires no external magnetic field can be of great importance, as it potentially paves the pathway for fabricating new types of devices based on the non-linear Hall effects. Some examples of current applications include (1) few-layer WTe₂ being used as a reading mechanism of the BC memory [45], (2) strain sensors for designing piezoelectric-like devices [46], and (3) current-rectification without semiconductor junctions [47].

Our analysis considering various 3D semimetals shows that MHE responses can be used as a complementary platform to map out various properties of semimetals, which can be used in conjunction with other probes [37, 48, 49]. One interesting direction will be to compute the effects of disorder [50, 51] and / or interactions [52–54]. However, a major impediment in these directions is that no consistent theory exists beyond the semiclassical approximation, which breaks down when quantum effects are robust. A possible way to make progress is to apply the invariant measure approach, which is currently being developed for simple transport properties [55].

[1] K. v. Klitzing, G. Dorda, and M. Pepper, New method for high-accuracy determination of the fine-structure constant based on quantized hall resistance, *Phys. Rev. Lett.* **45**, 494 (1980).

[2] Y. Chen, Y.-M. Lu, and H.-Y. Kee, Topological crystalline metal in orthorhombic perovskite iridates, *Nature Communications* **6**, 6593 (2015).

[3] T. Patlatiuk, C. P. Scheller, D. Hill, Y. Tserkovnyak, G. Barak, A. Yacoby, L. N. Pfeiffer, K. W. West, and D. M. Zumbühl, Evolution of the quantum Hall bulk spectrum into chiral edge states, *Nature Communications* **9**, 3692 (2018).

[4] M. Horsdal, M. Rypestøl, H. Hansson, and J. M. Leinaas, Charge fractionalization on quantum hall edges, *Phys. Rev. B* **84**, 115313 (2011).

[5] B. A. Bernevig, T. L. Hughes, and S.-C. Zhang, Quantum Spin Hall Effect and Topological Phase Transition in HgTe Quantum Wells, *Science* **314**, 1757 (2006).

[6] Z. Z. Du, H.-Z. Lu, and X. C. Xie, Nonlinear Hall effects, *Nature Reviews Physics* **3**, 744 (2021).

[7] G. Pacchioni, The Hall effect goes nonlinear, *Nature Reviews Materials* **4**, 514 (2019).

[8] K. Hamamoto, M. Ezawa, K. W. Kim, T. Morimoto, and N. Nagaosa, Nonlinear spin current generation in noncentrosymmetric spin-orbit coupled systems, *Phys. Rev. B* **95**, 224430 (2017).

[9] E. J. König, M. Dzero, A. Levchenko, and D. A. Pesin, Gyrotropic hall effect in berry-curved materials, *Phys. Rev. B* **99**, 155404 (2019).

[10] M. Papaj and L. Fu, Magnus hall effect, *Phys. Rev. Lett.* **123**, 216802 (2019).

[11] D. Mandal, K. Das, and A. Agarwal, Magnus nernst and thermal hall effect, *Phys. Rev. B* **102**, 205414 (2020).

[12] S. K. Das, T. Nag, and S. Nandy, Topological magnus responses in two- and three-dimensional systems, *Phys. Rev. B* **104**, 115420 (2021).

[13] C. Zeng, S. Nandy, A. Taraphder, and S. Tewari, Nonlinear nernst effect in bilayer wte₂, *Phys. Rev. B* **100**, 245102 (2019).

[14] X.-Q. Yu, Z.-G. Zhu, J.-S. You, T. Low, and G. Su, Topological nonlinear anomalous nernst effect in strained transition metal dichalcogenides, *Phys. Rev. B* **99**, 201410 (2019).

[15] T. Low, Y. Jiang, and F. Guinea, Topological currents in black phosphorus with broken inversion symmetry, *Phys. Rev. B* **92**, 235447 (2015).

[16] Z. Z. Du, C. M. Wang, H.-Z. Lu, and X. C. Xie, Band signatures for strong nonlinear hall effect in bilayer wte₂, *Phys. Rev. Lett.* **121**, 266601 (2018).

[17] I. Sodemann and L. Fu, Quantum nonlinear hall effect induced by berry curvature dipole in time-reversal invariant materials, *Phys. Rev. Lett.* **115**, 216806 (2015).

[18] J. I. Facio, D. Efremov, K. Koepernik, J.-S. You, I. Sodemann, and J. van den Brink, Strongly enhanced berry dipole at topological phase transitions in btei, *Phys. Rev. Lett.* **121**, 246403 (2018).

[19] Y. Zhang, Y. Sun, and B. Yan, Berry curvature dipole in weyl semimetal materials: An ab initio study, *Phys. Rev. B* **97**, 041101 (2018).

[20] K. Kang, T. Li, E. Sohn, J. Shan, and K. F. Mak, Nonlinear anomalous Hall effect in few-layer WTe₂, *Nature Materials* **18**, 324 (2019).

[21] P. He, S. S.-L. Zhang, D. Zhu, S. Shi, O. G. Heinonen, G. Vignale, and H. Yang, Nonlinear planar hall effect, *Phys. Rev. Lett.* **123**, 016801 (2019).

[22] X. Qian, J. Liu, L. Fu, and J. Li, Quantum spin hall effect in two-dimensional transition metal dichalcogenides, *Science* **346**, 1344 (2014).

[23] E. McCann and M. Koshino, The electronic properties of bilayer graphene, *Reports on Progress in Physics* **76**, 056503 (2013).

[24] M. Z. Hasan, S.-Y. Xu, I. Belopolski, and S.-M. Huang, Discovery of weyl fermion semimetals and topological fermi arc states, *Annual Review of Condensed Matter Physics* **8**, 289 (2017).

[25] R. Flores-Calderón and A. Martín-Ruiz, Quantized electrochemical transport in weyl semimetals, *Phys. Rev. B* **103**, 035102 (2021).

[26] M. Lundstrom, *Fundamentals of Carrier Transport*, 2nd ed. (Cambridge University Press, 2000).

[27] M. Dresselhaus, G. Dresselhaus, S. B. Cronin, and A. G. S. Filho, *Solid State Properties: From Bulk to Nano*, Graduate Texts in Physics (Springer-Verlag, Berlin Heidelberg, 2018).

[28] C. Fang, M. J. Gilbert, X. Dai, and B. A. Bernevig, Multi-weyl topological semimetals stabilized by point group symmetry, *Phys. Rev. Lett.* **108**, 266802 (2012).

[29] G. Xu, H. Weng, Z. Wang, X. Dai, and Z. Fang, Chern semimetal and the quantized anomalous hall effect in hgcr_2se_4 , *Phys. Rev. Lett.* **107**, 186806 (2011).

[30] S.-M. Huang, S.-Y. Xu, I. Belopolski, C.-C. Lee, G. Chang, T.-R. Chang, B. Wang, N. Alidoust, G. Bian, M. Neupane, D. Sanchez, H. Zheng, H.-T. Jeng, A. Bansil, T. Neupert, H. Lin, and M. Z. Hasan, New type of weyl semimetal with quadratic double weyl fermions, *Proceedings of the National Academy of Sciences* **113**, 1180 (2016).

[31] Q. Liu and A. Zunger, Predicted realization of cubic dirac fermion in quasi-one-dimensional transition-metal monochalcogenides, *Phys. Rev. X* **7**, 021019 (2017).

[32] P. Goswami and A. H. Nevidomskyy, Topological weyl superconductor to diffusive thermal hall metal crossover in the b phase of upt_3 , *Phys. Rev. B* **92**, 214504 (2015).

[33] M. H. Fischer, T. Neupert, C. Platt, A. P. Schnyder, W. Hanke, J. Goryo, R. Thomale, and M. Sigrist, Chiral d -wave superconductivity in srptas, *Phys. Rev. B* **89**, 020509 (2014).

[34] B. Roy, S. A. A. Ghorashi, M. S. Foster, and A. H. Nevidomskyy, Topological superconductivity of spin-3/2 carriers in a three-dimensional doped luttinger semimetal, *Phys. Rev. B* **99**, 054505 (2019).

[35] M. Trescher, B. Sbierski, P. W. Brouwer, and E. J. Bergholtz, Tilted disordered weyl semimetals, *Phys. Rev. B* **95**, 045139 (2017).

[36] I. Boettcher, Interplay of topology and electron-electron interactions in rarita-schwinger-weyl semimetals, *Phys. Rev. Lett.* **124**, 127602 (2020).

[37] S. Sekh and I. Mandal, Circular dichroism as a probe for topology in 3d semimetals (2021), arXiv:2105.05272 [cond-mat.mes-hall].

[38] D. Takane, Z. Wang, S. Souma, K. Nakayama, T. Nakamura, H. Oinuma, Y. Nakata, H. Iwasawa, C. Cacho, T. Kim, K. Horiba, H. Kumigashira, T. Takahashi, Y. Ando, and T. Sato, Observation of chiral fermions with a large topological charge and associated fermi-arc surface states in cosi, *Phys. Rev. Lett.* **122**, 076402 (2019).

[39] D. S. Sanchez, I. Belopolski, T. A. Cochran, X. Xu, J.-X. Yin, G. Chang, W. Xie, K. Manna, V. Süß, C.-Y. Huang, N. Alidoust, D. Multer, S. S. Zhang, N. Shumiya, X. Wang, G.-Q. Wang, T.-R. Chang, C. Felser, S.-Y. Xu, S. Jia, H. Lin, and M. Z. Hasan, Topological chiral crystals with helicoid-arc quantum states, *Nature* **567**, 500 (2019).

[40] Y. Liu, S. A. Yang, and F. Zhang, Circular dichroism and radial hall effects in topological materials, *Phys. Rev. B* **97**, 035153 (2018).

[41] Y. Chen, Y.-M. Lu, and H.-Y. Kee, Topological crystalline metal in orthorhombic perovskite iridates, *Nature Communications* **6**, 6593 (2015).

[42] N. P. Armitage, E. J. Mele, and A. Vishwanath, Weyl and dirac semimetals in three-dimensional solids, *Rev. Mod. Phys.* **90**, 015001 (2018).

[43] M.-X. Yang, H. Geng, W. Luo, L. Sheng, W. Chen, and D. Y. Xing, (2021), arXiv:2108.02338 [cond-mat.mes-hall].

[44] H. Gao, J. W. Venderbos, Y. Kim, and A. M. Rappe, Topological semimetals from first principles, *Annual Review of Materials Research* **49**, 153 (2019).

[45] D.-F. Shao, S.-H. Zhang, G. Gurung, W. Yang, and E. Y. Tsymbal, Nonlinear anomalous hall effect for néel vector detection, *Phys. Rev. Lett.* **124**, 067203 (2020).

[46] R.-C. Xiao, D.-F. Shao, Z.-Q. Zhang, and H. Jiang, Two-dimensional metals for piezoelectriclike devices based on berry-curvature dipole, *Phys. Rev. Applied* **13**, 044014 (2020).

[47] H. Isobe, S.-Y. Xu, and L. Fu, High-frequency rectification via chiral bloch electrons, *Science Advances* **6**, eaay2497 (2020).

[48] I. Mandal and K. Saha, Thermopower in an anisotropic two-dimensional weyl semimetal, *Phys. Rev. B* **101**, 045101 (2020).

[49] I. Mandal, Tunneling in Fermi systems with quadratic band crossing points, *Annals of Physics* **419**, 168235 (2020); Transmission in pseudospin-1 and pseudospin-3/2 semimetals with linear dispersion through scalar and vector potential barriers, *Physics Letters A* **384**, 126666 (2020); I. Mandal and A. Sen, Tunneling of multi-Weyl semimetals through a potential barrier under the influence of magnetic fields, *Physics Letters A* **399**, 127293 (2021); S. Bera and I. Mandal, Floquet scattering of quadratic band-touching semimetals through a time-periodic potential well, *Journal of Physics: Condensed Matter* **33**, 295502 (2021).

[50] B. Sbierski, M. Trescher, E. J. Bergholtz, and P. W. Brouwer, Disordered double weyl node: Comparison of transport and density of states calculations, *Phys. Rev. B* **95**, 115104 (2017); B. Sbierski, G. Pohl, E. J. Bergholtz, and P. W. Brouwer, Quantum transport of disordered weyl semimetals at the nodal point, *Phys. Rev. Lett.* **113**, 026602 (2014).

[51] R. M. Nandkishore and S. A. Parameswaran, Disorder-driven destruction of a non-fermi liquid semimetal studied by renormalization group analysis, *Phys. Rev. B* **95**, 205106 (2017); I. Mandal and R. M. Nandkishore, Interplay of coulomb interactions and disorder in three-dimensional quadratic band crossings without time-reversal symmetry and with unequal masses for conduction and valence bands, *Phys. Rev. B* **97**, 125121 (2018); I. Mandal, Robust marginal Fermi liquid in birefringent semimetals, *Physics Letters A* **418**, 127707 (2021).

[52] H. Rostami and V. Jurićć, Probing quantum criticality using nonlinear hall effect in a metallic dirac system, *Phys. Rev. Research* **2**, 013069 (2020).

[53] A. Avdoshkin, V. Kozii, and J. E. Moore, Interactions remove the quantization of the chiral photocurrent at weyl points, *Phys. Rev. Lett.* **124**, 196603 (2020).

[54] I. Mandal, Effect of Interactions on the Quantization of the Chiral Photocurrent for Double-Weyl Semimetals, *Symmetry* **12**, 919 (2020).

[55] I. Mandal and K. Ziegler, Robust quantum transport at particle-hole symmetry, *EPL (Europhysics Letters)* **135**, 17001 (2021).